Nuclear Science and Techniques (2026) 37:44
https://doi.org/10.1007/s41365-025-01872-4

Probing high-order deformation effects in neutron-deficient nuclei ^{246,248}No with improved potential-energy-surface calculations

Jin-Liang Guo[1] · Hua-Lei Wang[1] · Kui Xiao[1] · Zhen-Zhen Zhang[1] · Min-Liang Liu[2,3]

Received: 2 February 2025 / Revised: 21 April 2025 / Accepted: 29 April 2025 / Published online: 10 January 2026

Abstract
The high-order deformation effects in even–even ^{246,248}No are investigated by means of pairing self-consistent Woods–Saxon–Strutinsky calculations using the potential-energy-surface (PES) approach in an extended deformation space $(\beta_2, \beta_3, \beta_4, \beta_5, \beta_6, \beta_7, \beta_8)$. Based on the calculated two-dimensional projected energy maps and different potential energy curves, we found that the highly even-order deformations have an important impact on both the fission trajectory and energy minima, while the odd-order deformations, accompanying the even-order ones, primarily affect the fission path beyond the second barrier. Relative to the light actinide nuclei, the nuclear ground state changes to the superdeformed configuration, but the normally deformed minimum, as the low-energy shape isomer, may still be primarily responsible for enhancing nuclear stability and ensuring experimental accessibility in ^{246,248}No. Our present investigation indicates the nonnegligible impact of high-order deformation effects along the fission valley and will be helpful for deepening the understanding of different deformation effects and deformation couplings in nuclei, especially in this neutron-deficient heavy-mass region.

Keywords High-order deformations · Neutron-deficient nuclei · Potential energy surface · Nuclear stability · Macroscopic–microscopic model

1 Introduction

Determining the limits of nuclear stability and expanding the map of known isotopes are among the main goals of modern nuclear physics [1–3]. The single-particle structure is of great importance for nuclear stability, particularly for heavy nuclei. As it is known, the superheavy nuclei (with the atomic number $Z \geq 104$) exist only due to quantum shell effects originating from the non-uniform distribution of single-particle levels. Furthermore, the single-particle energies depend sensitively on the nuclear shape (equivalently, the nuclear mean field), which is usually parameterized by a set of deformation parameters. Therefore, it is necessary to treat deformations as accurately as possible, especially for heavy nuclear systems, in the theoretical description.

Indeed, the mechanism of spontaneous symmetry breaking allows nuclei to be represented as non-spherical shapes. Numerous experiments have indicated that nuclei can possess not only axially or nonaxially quadrupole deformations but also nonaxially or axially octupole and hexadecapole deformations [4–9]. Nuclear spectra, moments, and electromagnetic matrix elements are typically used to verify such deformation properties [4, 5, 10]. The importance of high-order deformation, e.g., the hexacontetrapole deformation β_6, has been revealed in describing the ground states [11–13] and the excited states including both the multi-quasiparticle high-K states [14, 15] and collective rotational states [15–18]. For instance, Xu et al. [18] recently probed the importance of the coupling between the

This work was supported by the Natural Science Foundation of Henan Province (No. 252300421478) and the National Natural Science Foundation of China (Nos. 11975209, U2032211, and 12075287). Some calculations were conducted at the National Supercomputing Center in Zhengzhou.

✉ Hua-Lei Wang
wanghualei@zzu.edu.cn

[1] School of Physics, Zhengzhou University, Zhengzhou 450001, China

[2] Key Laboratory of High Precision Nuclear Spectroscopy, Institute of Modern Physics, Chinese Academy of Sciences, Lanzhou 730000, China

[3] School of Nuclear Science and Technology, University of Chinese Academy of Sciences, Beijing 100049, China

high-order deformation β_6 and odd-order deformation β_3 in rotating ^{252,254}No. In the spontaneous fission process, the effect of higher multipolarity shape parameters in nuclei with $100 \leq Z \leq 114$ has also been revealed [19].

To date, the new generation of experimental facilities has served for many years to explore the limits of stability of high proton number (Z) and/or high isospin (T) nuclei, including the measurements of their structural properties. Theoretically, the main methods include macroscopic–microscopic (MM) models and microscopic theory, for example, cf. Refs. [20–22]. Prior to this work, we have performed some PES and total-Routhian-surface (TRS) calculations in multidimensional deformation spaces, e.g., $(\beta_2, \gamma, \beta_4)$, $(\beta_2, \beta_3, \beta_4, \beta_5)$ and some exotic deformation spaces [5–7, 9, 23–26]. In the present study, using an improved PES calculation with the inclusion of higher multipolarity deformations, we focus on investigating the ^{246,248}No nuclei, located in both the heavy and drip-line actinide regions. The ^{248}No nucleus is the most neutron-deficient even–even No isotope, which has already been synthesized experimentally [27], but the half-life and structural properties remain unknown, and its neighboring even–even ^{246}No nucleus is expected to be synthesized as the next candidate. In Ref. [28], it was reported that a large reduction of more than five and six orders of magnitude of the ground-state fission half-lives was found between ^{252}No and ^{254}No and, following this trend, the fission half-life of the ground state of the more neutron-deficient even–even No isotopes will be extremely short, making it experimentally inaccessible and very close to the 10^{-14}-s limit of existence of an atom. However, a recent study within a cluster model pointed out that the neutron-deficient ^{247,248}No nuclei are relatively stable with respect to spontaneous fission, and no abrupt decreases in their fission half-lives were observed [29].

Concerning the development of the PES approach, our primary contribution in this work is to extend the deformation space $(\beta_2, \beta_3, \beta_4, \beta_5)$ to further cover higher-order β_6, β_7 and β_8 degrees of freedom, mainly including the calculation modifications of the new Hamiltonian matrix, surface, and Coulomb energies of the nuclear liquid drop. The remainder of this paper is organized as follows. The theoretical framework is described in Sect. 2. The calculated results and related discussions are presented in Sect. 3. Finally, Sect. 4 summarizes the main conclusions of this study.

2 Theoretical method

The general procedures for PES calculations (even with rotation, e.g., TRS) within the framework of MM models are standard and have been summarized in Refs. [30–32]. In the following, we briefly present the realization of the PES approach, focusing on the leading lines and some basic definitions.

First, let us briefly review one of the widely used techniques for nuclear shape (potential) parameterization. Namely, one can define the nuclear surface in terms of the spherical-harmonic basis expansion as,

$$\Sigma : R(\theta, \phi) = R_0 c(\alpha)\Big[1 + \sum_{\lambda} \sum_{\mu=-\lambda}^{+\lambda} \alpha_{\lambda\mu} Y_{\lambda\mu}(\theta, \phi)\Big], \tag{1}$$

where the expansion coefficients $\alpha_{\lambda\mu}$ are usually called "deformation parameters" (also, "deformations" in short). The ensemble of all the adopted deformation parameters $\{\alpha_{\lambda\mu}\}$ is usually abbreviated as α. The radius parameter $R_0 = r_0 A^{1/3}$ (where $r_0 = 1.2$ fm) provides an approximation of the effective nuclear spherical radius in Fermi, and the auxiliary function $c(\alpha)$ ensures the conservation of the nuclear volume; for example, the volume enclosed by the nuclear surface Σ is equal to the volume of the corresponding spherical nucleus (independent of the actual shape). To avoid possible confusion, it is worth noting that, similar to the coordinate space, a vector can be projected onto the axes; in the deformation space expanded by spherical harmonics, the total deformation β and deformation β_λ at λ order are usually defined by $\beta = \sqrt{\sum_\lambda \beta_\lambda^2}$ and $\beta_\lambda = \sqrt{\sum_\mu \alpha_{\lambda\mu}^2}$, respectively [33, 34]. For the axially symmetric shape, such as that considered in this project, the deformation β_λ equals $\alpha_{\lambda 0}$ owing to $\alpha_{\lambda\mu\neq 0} = 0$. In this study, we consider the deformation degrees of freedom $\beta_{6,7,8}$ and spherical harmonics $Y_{\lambda_{6,7,8}\mu=0}$, that is, see Eq. (1), extending the deformation space $(\beta_2, \beta_3, \beta_4, \beta_5)$ to $(\beta_2, \beta_3, \beta_4, \beta_5, \beta_6, \beta_7, \beta_8)$.

The phenomenological nuclear potential can be calculated using a parameterized nuclear shape. For a nucleus, the Woods–Saxon (WS) potential is more realistic owing to its flat-bottomed and short-range properties. In the project, we numerically solve the Schrödinger equation with a deformed WS Hamiltonian [35, 36],

$$\hat{H}_{\rm WS} = \hat{T} + \hat{V}_{\rm cent} + \hat{V}_{\rm so} + \hat{V}_{\rm Coul}, \tag{2}$$

where the central part of the WS potential reads

$$\hat{V}_{\rm cent}(\vec{r}, \beta; V_0, r_0, a_0) = \frac{V_0[1 \pm \kappa(N-Z)/(N+Z)]}{1 + \exp[{\rm dist}_\Sigma(\vec{r}, \beta; r_0)/a_0]}, \tag{3}$$

where the plus and minus signs hold for protons and neutrons, respectively, and the parameter a_0 denotes the surface diffuseness. The parameters V_0 and r_0 represent the central potential depth and central potential radius parameters, respectively. The term ${\rm dist}_\Sigma(\vec{r}, \beta; r_0)$ represents the distance of a point $\vec{r}$ from nuclear surface Σ. The spin-orbit potential, which strongly affects the level order and depends on

the gradient of the central potential with new parameters, is defined by

$$\hat{V}_{\rm so}(\vec{r},\hat{p},\hat{s},\beta;\lambda,r_{\rm so},a_{\rm so}) = -\lambda\left[\frac{\hbar}{2mc}\right]^2 \nabla V^{\rm so}\times\hat{p}\cdot\hat{s}, \tag{4}$$

where

$$V^{\rm so}(\vec{r},\beta;r_{\rm so},a_{\rm so}) = \frac{V_0[1\pm\kappa(N-Z)/(N+Z)]}{1+\exp[{\rm dist}_{\Sigma_{\rm so}}(\vec{r},\beta;r_{\rm so})/a_{\rm so}]}, \tag{5}$$

The parameter λ denotes the strength of the effective spin-orbit force acting on individual nucleons. It should be stressed that the new surface $\Sigma_{\rm so}$ is different from that in Eq. (3) due to the different radius parameters $r_{\rm so}$. In addition, the spin-orbit diffusivity parameter $a_{\rm so}$ is usually updated.

For protons, a classical electrostatic potential of a uniformly charged drop is used for describing the Coulomb potential, which is defined as

$$V^{\rm Coul}(\vec{r},\beta) = Ze\int_{\Sigma}\frac{{\rm d}^3\vec{r'}}{|\vec{r}-\vec{r'}|}, \tag{6}$$

where the integration extends over the volume delimited by surface Σ.

During the process of calculating the WS Hamiltonian matrix, we use the eigenfunctions of the axially deformed harmonic oscillator potential in the cylindrical coordinate system as the basis function, as seen below,

$$|n_\rho n_z\Lambda\Sigma\rangle = \psi^{\Lambda}_{n_\rho}(\rho)\psi_{n_z}(z)\psi_\Lambda(\varphi)\chi(\Sigma). \tag{7}$$

For more details, one can see Ref. [36]. The eigenfunctions with $N\leqslant 12$ and 14 are chosen as the basis set for protons and neutrons, respectively. The corresponding single-particle levels (eigenvalues) and wave functions (eigenvectors) are obtained by diagonalizing the Hamiltonian matrix. It was found that, using such a cutoff, the calculated results (e.g., single-particle energies) were sufficiently stable with respect to a possible enlargement of the basis space.

Based on the obtained single-particle levels at the corresponding nuclear shape, the quantum shell correction and pairing-energy contributions can be further calculated using the Strutinsky method [37] and the Lipkin–Nogami (LN) method [38, 39]. In these methods, the microscopic shell-correction energy is given by

$$\delta E_{\rm shell}(Z,N,\hat{\beta}) = \sum e_i - \int e\tilde{g}(e){\rm d}e, \tag{8}$$

where e_i denotes the calculated single-particle levels and $\tilde{g}(e)$ is the smooth level density. The smoothed distribution function $\tilde{g}(e)$ was earlier defined as

$$\tilde{g}(e,\gamma) \equiv \frac{1}{\gamma\sqrt{\pi}}\sum_i \exp\left[-\frac{(e-e_i)^2}{\gamma^2}\right], \tag{9}$$

where γ denotes the smoothing parameter. To eliminate any possibly strong dependence of the γ-parameter, the level density $\tilde{g}(e)$, optimized by a curvature-correction polynomial $P_{\rm p}(x)$, is usually given by [37, 40–42],

$$\tilde{g}(e,\gamma,p) = \frac{1}{\gamma\sqrt{\pi}}\sum_{i=1} P_{\rm p}\left(\frac{e-e_i}{\gamma}\right)\times\exp\left[-\frac{(e-e_i)^2}{\gamma^2}\right]. \tag{10}$$

The corrective polynomial $P_{\rm p}(x)$ can be expanded in terms of Hermite or Laguerre polynomials. The expanded coefficients can be obtained using the orthogonality properties of these polynomials and the Strutinsky condition [43]. In the present work, a sixth-order Hermite polynomial and a smoothing parameter $\gamma = 1.20\hbar\omega_0$, where $\hbar\omega_0 = 41/A^{1/3}$ MeV, are adopted [37].

In addition to the shell correction, another important quantum correction is the pairing-energy contribution. It is worth noting that various pairing-energy variants exist in the MM approach [44]. Several types of phenomenological expressions have been widely adopted, such as pairing correlation and pairing correction energies, employing or not employing the particle number projection technique. We employ the LN method, an approximate particle number projection technique, to treat the pairing-energy calculation [38, 39]. Such a pairing treatment can help avoid not only the spurious pairing phase transition but also the particle number fluctuations encountered in simpler BCS calculations. In this method, the LN pairing energy for an even–even nucleon system at "paired solution" (pairing gap $\Delta\neq 0$) is calculated by [20, 38]

$$E_{\rm LN} = \sum_k 2{v_k}^2 e_k - \frac{\Delta^2}{G} - G\sum_k {v_k}^4 - 4\lambda_2\sum_k {u_k}^2{v_k}^2, \tag{11}$$

where ${v_k}^2$, e_k, Δ, and λ_2 represent the occupation probabilities, single-particle energies, pairing gap, and number-fluctuation constant, respectively. The monopole pairing strength G is determined using the average gap method [30]. For the case of "no-pairing solution" ($\Delta = 0$), its partner expression is

$$E_{\rm LN}(\Delta=0) = \sum_k 2e_k - G\frac{N}{2}. \tag{12}$$

The difference between paired solution $E_{\rm LN}$ and no-pairing solution $E_{\rm LN}(\Delta=0)$ is usually referred to as the pairing correlation, which can be written as,

$$\delta E_{\text{pair}} = \sum_k 2{v_k}^2 e_k - \frac{\Delta^2}{G} - G\sum_k {v_k}^4 - 4\lambda_2 \sum_k {u_k}^2 {v_k}^2 + G\frac{N}{2} - \sum_k 2e_k. \tag{13}$$

Following Refs. [12, 20], we define the total microscopic energy as

$$E_{\text{micro}}(Z,N,\beta) = \delta E_{\text{shell}}(Z,N,\beta) + \delta E_{\text{pair}}(Z,N,\beta). \tag{14}$$

This definition is equivalent to the concept of "shell correction" δE_{shell} ($\equiv E_{\text{LN}} - \tilde{E}_{\text{Strut}}$), cf. Equation (1) in Ref. [30], merging the quantum shell correction and pairing contributions. For clarifying some confusing points, we would like to point out that in Ref. [30], the definition of E_{LN} includes the term $G\frac{N}{2}$. It should be mentioned that the microscopic energy includes the proton distributions of protons and neutrons simultaneously.

The macroscopic energy can be calculated using the standard liquid-drop model [33]. Since we pay attention to the deformation effects instead of, e.g., masses, in the PES calculation, the deformation liquid-drop energy (relative to the spherical liquid drop) is adopted [33, 36, 37], as seen below,

$$E_{\text{macro}}(Z,N,\beta) = E_{\text{ld}}(Z,N,\beta) = \{[B_{\text{S}}(\beta) - 1] + 2\chi[B_{\text{C}}(\beta) - 1]\}E_{\text{S}}^{(0)}, \tag{15}$$

where the spherical surface energy $E_{\text{S}}^{(0)}$ and fissility parameter χ are Z and N-dependent, respectively [33, 37]. The relative surface and Coulomb energies B_{S} and B_{C} are functions of the nuclear shape.

Within the framework of MM model, the total energy can be calculated by [20, 45]

$$E_{\text{total}}(Z,N,\beta) = E_{\text{macro}}(Z,N,\beta) + E_{\text{micro}}(Z,N,\beta). \tag{16}$$

Once the total energy is obtained at each sampling deformation grid, we can obtain a smooth potential energy surface/map with the help of interpolation techniques, such as a spline function, and then investigate nuclear properties, including the equilibrium deformations, shape coexistence, fission path, and other physical quantities/processes.

3 Results and discussion

In this project, we restricted ourselves to axially symmetric shapes and performed numerical calculations in a seven-dimensional deformation space. Namely, we calculate (25, 13, 13, 7, 5, 5, 5) points for ($\beta_2, \beta_3, \beta_4, \beta_5, \beta_6, \beta_7, \beta_8$) deformations, respectively, taking the size 0.05 as the deformation step. Our primary concern is how high-order multipolarity deformations and their couplings affect the potential energy landscapes.

For heavy nuclear systems, nuclear stability is approximately governed by the competition between the surface tension of the nuclear liquid drop and the strong Coulomb repulsion between numerous protons. The former tends to hold the system together, whereas the latter drives the nucleus toward spontaneous fission. To understand the influence of different deformation parameters on the macroscopic energy, taking ^{248}No as an example, the evolution of deformed liquid-drop energies near the spherical and elongated shapes is illustrated in Fig. 1. For such a heavy nucleus, the macroscopic liquid-drop energy remains almost a small constant with changing β_2, in agreement with our previous study [6]. It can be observed that the nuclear stiffness (usually defined by $\partial E_{\text{ld}}/\partial\beta_\lambda$) near the spherical shape increases with increasing λ, as shown in Fig. 1a, indicating that it is more difficult to achieve higher-order deformations. However, for the elongated case, for example, $\beta_2 = 1.0$, cf. Figure 1b, the nuclear shape becomes soft along the direction of each deformation degree of freedom. In particular, as shown in Fig. 1b, the stable β_4 deformation appears under the circumstances. Even the stiffnesses along β_7 and β_8 are

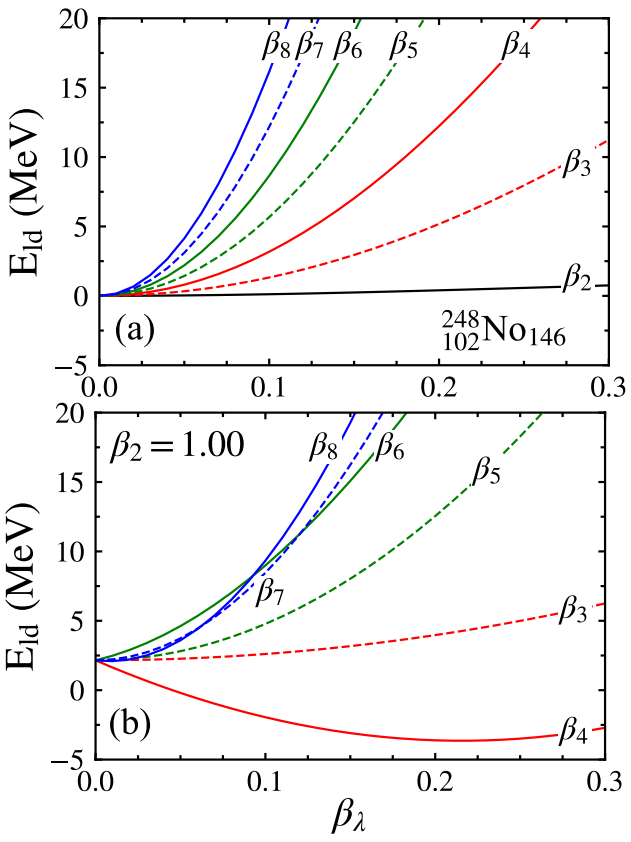

Fig. 1 (Color online) Macroscopic deformation energies as functions of separate deformations β_λ for ^{248}No, $\lambda = 2, 3, 4, 5, 6, 7, 8$. Note that, different from **a**, the β_2 deformation is fixed to 1.0 in subfigure **b**

almost the same and smaller than that along the lower-order deformation β_6 at approximately $\beta_{6,7,8} < 0.1$, which means that high-order $\beta_{7,8}$ deformations may be more favored than β_6. In practical calculations, the different couplings of different deformations may be complex.

Quantum shell effects arising from single-particle states can enhance nuclear stability in the MM calculation because high and low densities will give rise to positive and negative shell corrections, respectively. The appearance of these appropriate corrections on the pathway to scission may lead to enhanced stability. Figure 2 shows the effects of different high-order deformations (e.g., $\lambda \geq 5$) on microscopic single-particle energies (not far from the Fermi surface) for neutrons (similarly, for protons) in the example nucleus ^{248}No, indicating the success of the modified PES approach. The neutron spherical shell gaps at $Z = 126$, 164, and 184 are reproduced from the single-particle energy diagram. The single-particle levels as a function of low-order deformations (e.g., β_2, γ and β_4) can be easily found in the literature [23].

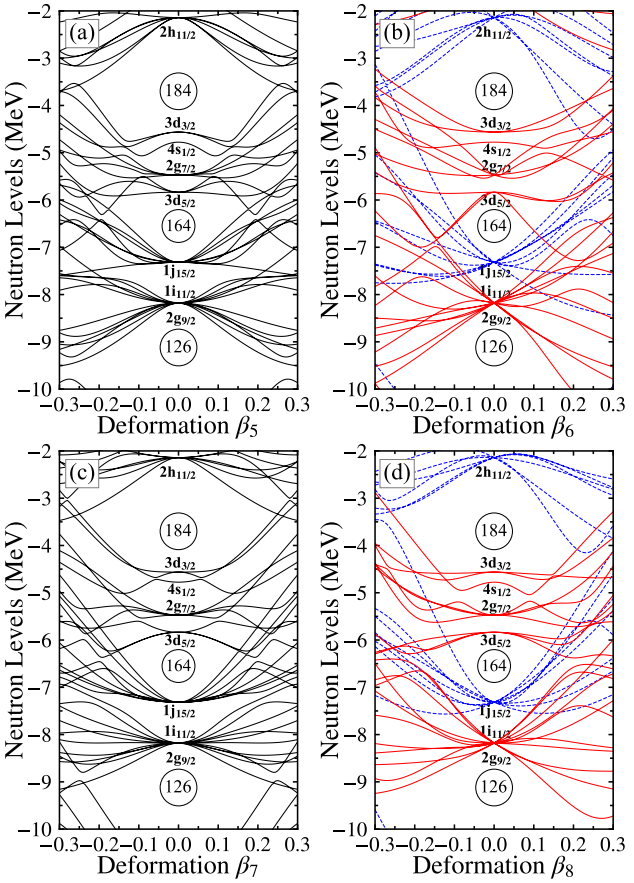

Fig. 2 (Color online) Neutron single-particle energies as functions of separate deformation β_5 **a**, β_6 **b**, β_7 **c**, and β_8 **d** for ^{248}No. For each subplot, the other deformation parameters are set to zero, and the spherical quantum numbers *nlj* are given as labels. In **b** and **d**, the solid red and dash blue lines indicate the positive and negative-parity levels, respectively

It is worth noting that the nucleus with odd λ deformation possesses the same shapes (namely the same nuclear potential but different orientation) for positive and negative β_λ values; the Hamiltonian of the nuclear system will satisfy the relation $\hat{H}(-\beta_{\lambda_{\rm odd}}) = \hat{H}(+\beta_{\lambda_{\rm odd}})$ such that the single-particle diagram is symmetric about positive and negative $\beta_{\lambda_{\rm odd}}$ values. Of course, it can be easily imagined that, for the separate deformation $\beta_{\lambda_{\rm odd}}$, the macroscopic liquid-drop energy $E_{\rm ld}$ also satisfies $E_{\rm ld}(+\beta_{\lambda_{\rm odd}}) = E_{\rm ld}(-\beta_{\lambda_{\rm odd}})$ since the atomic nucleus at this moment just has the different spatial orientations. It may be somewhat complex to combine several odd-λ deformations, but one can determine the symmetry relations. For instance, the three-dimensional subspace $(\beta_3, \beta_5, \beta_7)$ can be divided into eight sections (quadrants). The potential energies at the lattices $(+\beta_3, +\beta_5, +\beta_7)$ and $(-\beta_3, -\beta_5, -\beta_7)$ will be equal because the nuclear shapes are identical at these two types of deformation grids, abbreviated to $(+,+,+)$ and $(-,-,-)$ for short. Similarly, the other three pairs of symmetric combinations are $(+,+,-)$ and $(-,-,+)$, $(+,-,-)$ and $(-,+,+)$, $(-,+,-)$, and $(+,-,+)$. Such symmetry reduces the number of calculated deformation grids by half.

All projected two-dimensional β_2 vs β_λ ($\lambda = 3, 4, 5, 6, 7$ or 8) maps for ^{246}No and ^{248}No in such a seven-dimensional deformation space are illustrated in Figs. 3 and 4. In each subplot, the total energy is minimized over the remaining deformation degrees of freedom (e.g., on the β_2 vs β_3 plane, the energy is minimized over $\beta_{4,5,6,7,8}$). From these projection maps, some properties, such as energy minima and fission paths, can be analyzed. It should be noted that, ignoring the interpolated errors, the corresponding minima, for example, the normally deformed minima near $\beta_2 = 0.2$ and the superdeformed minima near $\beta_2 = 0.7$, in different projection maps are the same. In these two figures, all odd-order deformation parameters are zero at both the normally deformed and superdeformed minima. The ensembles $(\beta_2, \beta_4, \beta_6, \beta_8; E_{\rm min})$ are, respectively (0.234, 0.041, −0.017, −0.005; −5.82 MeV) and (0.679, 0.045, −0.005, −0.007; −7.08 MeV), for the normally deformed and superdeformed minima in Fig. 3 [similarly, (0.242, 0.033, −0.021, −0.007; −6.33 MeV) and (0.679, 0.037, −0.003, −0.007; −7.12 MeV) in Fig. 4]. Because there is no experimental deformation information for these two nuclei, it is instructive to compare our calculations (or part of them) with other theories. Indeed, the equilibrium deformations of the normally deformed minima calculated in this study are in good agreement with the results of Möller et al. [20]. In Ref. [20], nuclear ground-state deformations are calculated in the deformation space $\{\beta_\lambda; \lambda = 2, 3, 4, 6\}$ based on the finite-range droplet macroscopic model and folded-Yukawa single-particle microscopic model; the calculated $(\beta_2, \beta_3, \beta_4, \beta_6)$ values are (0.224, 0.00, 0.054, −0.025) and (0.235, 0.00, 0.048, −0.033), respectively, which agree

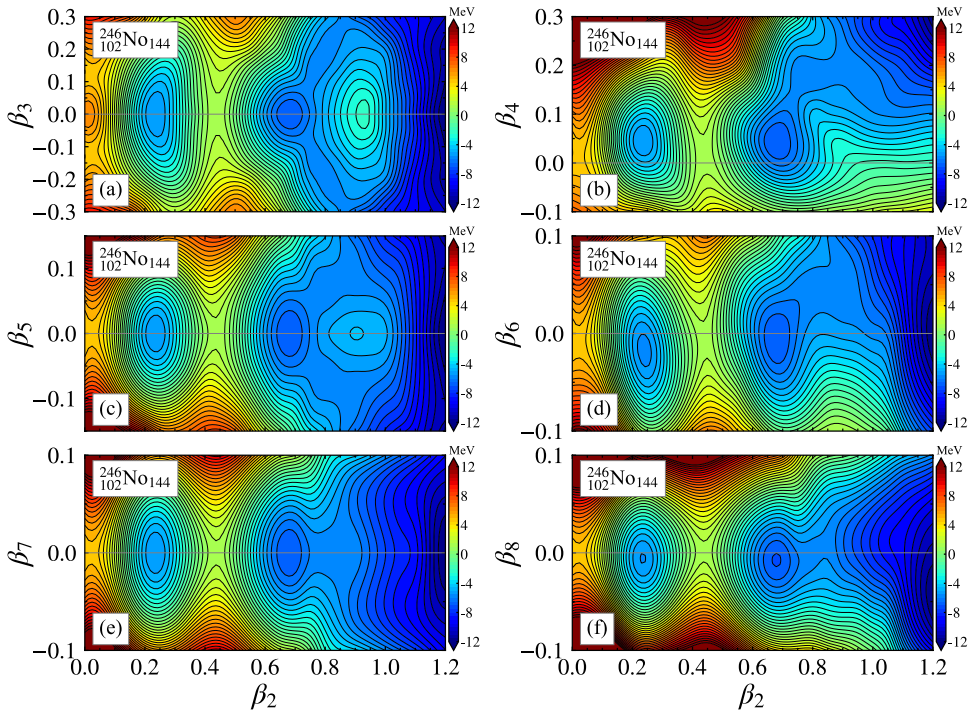

Fig. 3 (Color online) Potential energy projections on (β_2, $\beta_{\lambda=3,4,5,6,7,8}$) planes, contour-line separation of 0.5 MeV, minimized at each deformation point over other deformations, for the ^{246}No nucleus. For more details, see the text

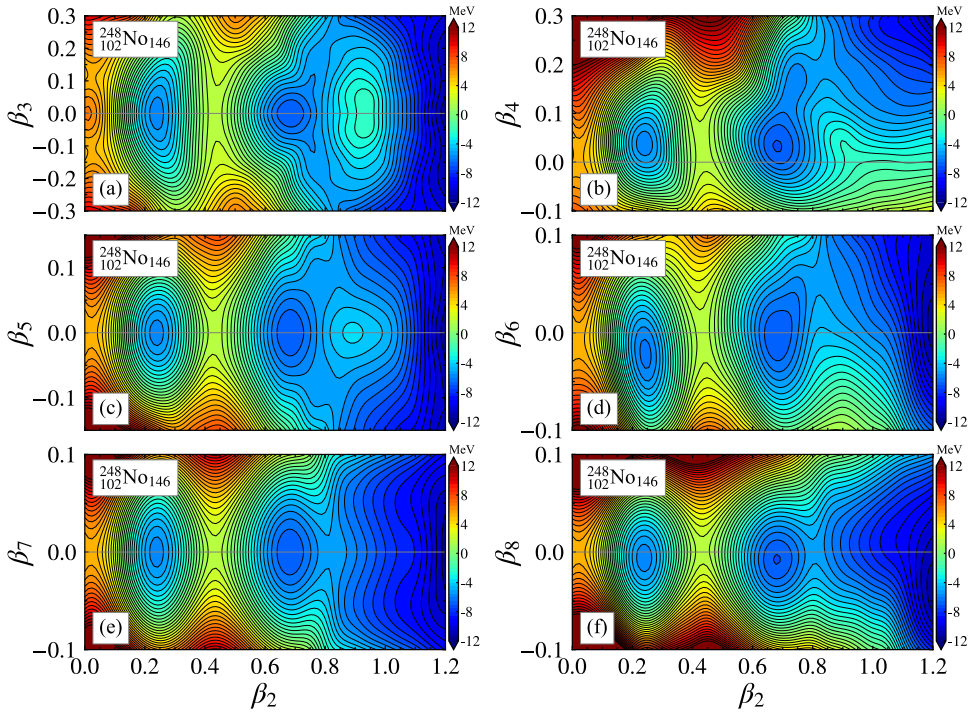

Fig. 4 (Color online) Similar to Fig. 3, but for the ^{248}No nucleus

with the present results, as shown in Figs. 3 and 4. Furthermore, our calculations indicate that besides β_4 and β_6, the even-order deformation β_8 has a slight impact on the normally deformed minima in these two nuclei. In addition, one can see that all the even-order deformations affect the superdeformed energy minima to some extent. In particular, it seems that the impact of high-order deformation β_8 is more important than that of β_6, which agrees with the case illustrated in Fig. 1b (in the strongly elongated situation, the nucleus may be softer along β_8 than β_6). Concerning the odd-order deformations β_3, β_5 and β_7, we find that they do not affect both the normally deformed and the superdeformed minima but affect the saddle-point positions and fission paths after the superdeformed minima.

To understand the effects of even- and odd-order deformations on the fission trajectory, Fig. 5 shows four types of potential energy curves along the minimum valley in the quadrupole deformation β_2 direction for ^{246,248}No. The typically double-humped fission barriers in actinide nuclei are well reproduced [46]. Note that the $E(\beta_2)$ curves I and IV will, respectively, occupy the highest and lowest positions at each β_2 point since the former minimizes over {none} but the latter over $\{\beta_\lambda; \lambda = 3, 4, 5, 6, 7, 8\}$. Keeping this in mind, one can easily read this figure, although there is a strong overlap of different curves. Curve II, which is minimized over the remaining even-order deformations $\beta_{4,6,8}$, further decreases the energies of the normally deformed minimum and the superdeformed minimum, leading to the formation of the second barrier. Indeed, only considering the deformation β_2, for example, curve I, the energy will continue to increase after the superdeformed minimum with the increase of β_2 (at least, up to $\beta_2 = 1.2$). Except for the weak deformation region (e.g., approximately $\beta_2 \leq 0.1$), the energy curves I and III fully overlap, indicating that there are no odd-order deformation effects along the fission valley in the deformation subspace $(\beta_2, \beta_3, \beta_5, \beta_7)$. Similarly, the overlap of energy curves II and IV before $\beta_2 \approx 0.8$ also illustrates such negligible odd-order deformation effects. Comparing curves II and IV, we find that the inclusion of odd-order deformations further decreases the second barrier, indicating the occurrence of coupling between odd- and even-order deformations. The properties of the potential energy curves are similar for subplots (a) ^{246}No and (b) ^{248}No, except for a slightly lower outer barrier in ^{246}No. It is known that both spontaneous fission and α decay, which terminate the stability of drip-line heavy nuclei, sensitively depend on such potential energy curves. With a decrease in the neutron number, ^{246}No is excepted to have a shorter half-life than ^{248}No; however, there should be no abrupt reduction according to the fission trajectories. It is instructive to investigate the evolution properties of single-particle energies and macroscopic and microscopic energies along the "realistic" fission path (corresponding to curve IV in Fig. 5). Accordingly, the representative single-neutron diagram and different energy curves are illustrated for ^{248}No (and similarly for ^{246}No) in Fig. 6. It can be observed that the single-particle levels involving different deformations become more complicated, as shown in Fig. 6a. From Fig. 6b, the formation of the inner barrier primarily originates from the microscopic shell correction, and the outer barrier is strongly affected by the macroscopic liquid-drop energy and microscopic shell correction. The pairing correlation always provides a negative and relatively smoothed energy.

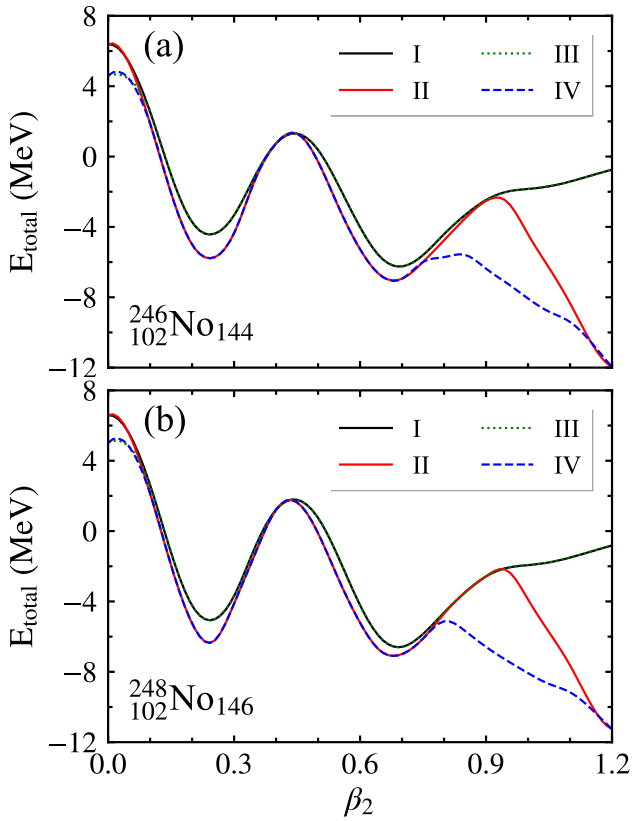

Fig. 5 (Color online) Four types of potential energy curves as the function of deformation β_2 for ^{246}No **a** and ^{248}No **b**. At each β_2 point, the energy minimization was performed over {none} (I; solid black line), $\{\beta_\lambda; \lambda = 4, 6, 8\}$ (II; solid red line), $\{\beta_\lambda; \lambda = 3, 5, 7\}$ (III; dotted green line), and $\{\beta_\lambda; \lambda = 3, 4, 5, 6, 7, 8\}$ (IV; dash blue line). See text for further explanations

It should be pointed out that although the normally deformed minimum in ^{246,248}No is still referred to as the ground state in Ref. [20], the inversion of the energies between the normally deformed minimum and the superdeformed minimum has occurred. Therefore, strictly speaking, the superdeformed minima in ^{246,248}No are the ground states. The fission half-lives of ^{246,248}No decaying from such ground states will rapidly decrease relative to those of normally deformed ground states (e.g., in lighter actinide nuclei). However, as discussed in Ref. [47] where it is pointed out that the stability of superheavy nuclei may be enhanced by high-K isomer, such very neutron-deficient heavy nuclei may have the enhanced stability due to the normally deformed minimum as the shape isomer. (The study of decay half-life from it, including the typical γ distortion of the inner barrier [23], is beyond the scope of the present work.)

In addition, to verify that odd-order deformation effects for the fission paths can occur only when the even-order deformations are considered, we show the energy projection maps in the (β_2, β_3) plane for ^{246,248}No in Fig. 7, ignoring the even-order deformation degrees of freedom. The fission valley in Fig. 7 is equivalent to curve III in Fig. 5. From Fig. 7, one can see that, from the normally deformed minima to the strongly elongated region, the odd-order deformation β_3 does not change the fission path in ^{246,248}No. It can be concluded

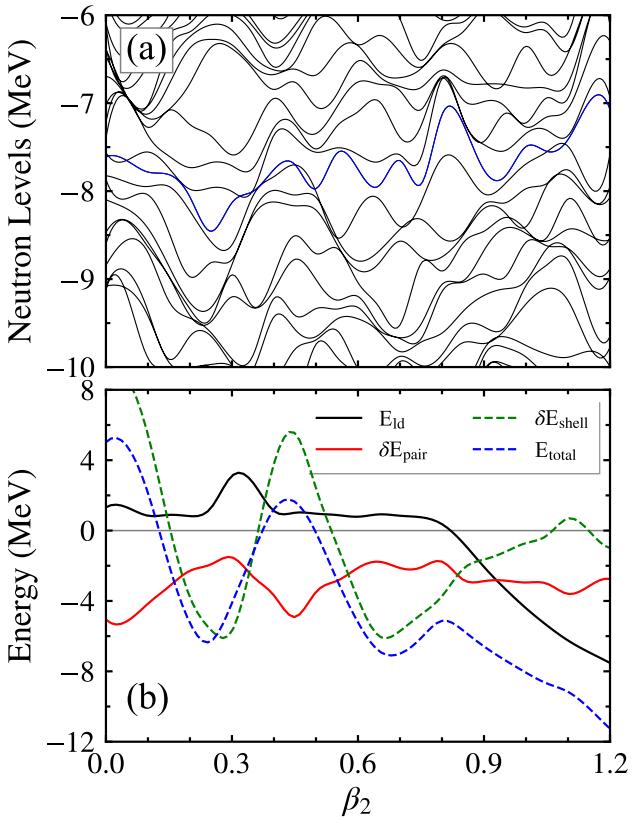

Fig. 6 (Color online) Neutron single-particle levels **a** and different energy curves (total energy and its macroscopic and microscopic components) in functions of β_2 for the nucleus ^{248}No. Note that for **a** and **b**, at each β_2 grid, other deformation parameters adopt the values after the energy minimization, and the total energy curve in **b** is the same as curve IV in Fig. 5. In subplot **a**, the energy level with blue color denotes the Fermi level

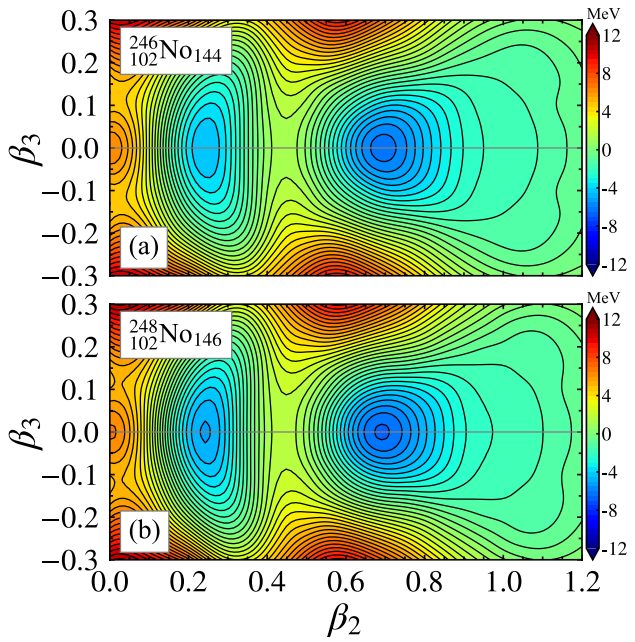

Fig. 7 (Color online) Similar to Figs. 3a and 4a, potential energy projections on (β_2, β_3) plane for ^{246}No **a** and ^{248}No **b**. But, in each subplot, the minimization is performed over β_5 and β_7, without the consideration of even-order deformations

that odd-order deformation effects only play important roles, accompanied by higher even-order deformations (e.g., β_4). Whether such a conclusion is a general rule deserves further study through systematic investigation in the future.

4 Summary

In this project, we developed a PES calculation method, extending the deformation space, within the framework of the MM model and investigated the high-order deformation effects in the neutron-deficient heavy nuclei ^{246,248}No. The evolution properties of microscopic single-particle levels and macroscopic energies as functions of different deformation degrees of freedom are illustrated. It was found that the higher the deformation order, the more difficult it is to occur because, for a spherical liquid drop, in general, the stiffness along some deformation will gradually increase as the corresponding deformation multipolarity increases. However, for a strongly elongated spheroid, high-order deformations play an important role owing to the large softness along them. Our calculations illustrate that the highly even-order deformations significantly affect both the potential energy minima and the fission paths. In particular, the high-order deformation β_8 may be more favored than the lower-order β_6 for a strongly elongated nuclear shape. All odd-order deformations mainly affect the second barrier, but they must accompany even-order deformations (e.g., β_4). Indeed, the inclusion of higher-order deformations is somewhat necessary in the study of nuclear structure, nuclear fusion, and fission processes. Although we cannot accurately determine the symmetry properties of fission fragments owing to the scarcity of information on the scission points, the trend in earlier studies [48, 49] indicates the possible occurrence of asymmetric fissions in these two nuclei. Moreover, it is also found that the very neutron-deficient ^{246}No nucleus may still be accessed experimentally because, similar to the high-K isomer reported in Ref. [47], the normally deformed shape isomer can enhance the survival probability in the drip-line heavy nucleus, although the super-deformed ground state is rather unstable. In the future, it would be meaningful to extend the deformation space to include nonaxially deformations.

Author contributions All authors contributed to the study conception and design. Material preparation and data collection and analysis were performed by Jin-Liang Guo, Hua-Lei Wang, Kui Xiao, Zhen-Zhen Zhang, and Min-Liang Liu. The first draft of the manuscript

was written by Jin-Liang Guo, and all authors commented on previous versions of the manuscript. All authors read and approved the final manuscript.

Data availability The data that support the findings of this study are openly available in Science Data Bank at https://cstr.cn/31253.11.sciencedb.j00186.00795 and https://doi.org/10.57760/sciencedb.j00186.00795.

Declarations

Conflict of interest The authors declare that they have no conflict of interest.

References

1. M. Wang, W. Huang, F. Kondev et al., The AME 2020 atomic mass evaluation (II). tables, graphs and references. Chin. Phys. C **45**, 030003 (2021). https://doi.org/10.1088/1674-1137/abddaf
2. G.P. Liu, H.L. Wang, Z.Z. Zhang et al., Model-repair capabilities of tree-based machine-learning algorithms applied to theoretical nuclear mass models. Phys. Rev. C **111**, 024306 (2025). https://doi.org/10.1103/PhysRevC.111.024306
3. M.T. Wan, L. Ou, M. Liu et al., Properties of the drip-line nucleus and mass relation of mirror nuclei. Nucl. Sci. Tech. **36**, 26 (2025). https://doi.org/10.1007/s41365-024-01633-9
4. P.A. Butler, W. Nazarewicz, Intrinsic reflection asymmetry in atomic nuclei. Rev. Mod. Phys. **68**, 349–421 (1996). https://doi.org/10.1103/RevModPhys.68.349
5. H.L. Wang, H.L. Liu, F.R. Xu et al., Investigation of octupole effects in superheavy nuclei with improved potential-energy-surface calculations. Chin. Sci. Bull. **57**, 1761–1764 (2012). https://doi.org/10.1007/s11434-012-5118-y
6. T.T. Li, H.L. Wang, Z.Z. Zhang et al., Probing the structural evolution along the fission path in the superheavy nucleus ^{256}Sg. Indian J. Phys. **97**, 2793–2808 (2023). https://doi.org/10.1007/s12648-023-02626-x
7. Z. Song, H.L. Wang, Z.Z. Zhang et al., Probes of axial and nonaxial hexadecapole deformation effects in nuclei around ^{230}U. Commun. Theor. Phys. **75**, 025303 (2023). https://doi.org/10.1088/1572-9494/acae80
8. B. Schenke, Violent collisions can reveal hexadecapole deformation of nuclei. Nucl. Sci. Tech. **35**, 115 (2024). https://doi.org/10.1007/s41365-024-01509-y
9. X.Y. Wei, H.L. Wang, Z.Z. Zhang et al., Revisiting the island of hexadecapole-deformation nuclei in the $A \approx 150$ mass region: Focusing on the model application to nuclear shapes and masses. Commun. Theor. Phys. **76**, 025301 (2024). https://doi.org/10.1088/1572-9494/ad19d7
10. F.S. Stephens, F. Asaro, I. Perlman, Radiations from 1- states in even-even nuclei. Phys. Rev. **100**, 1543–1545 (1955). https://doi.org/10.1103/PhysRev.100.1543
11. Z. Patyk, A. Sobiczewski, Main deformed shells of heavy nuclei studied in a multidimensional deformation space. Phys. Lett. B **256**, 307–310 (1991). https://doi.org/10.1016/0370-2693(91)91766-O
12. P. Möller, A. Sierk, T. Ichikawa et al., Nuclear ground-state masses and deformations: FRDM(2012). At. Data Nucl. Data Tables **109–110**, 1–204 (2016). https://doi.org/10.1016/j.adt.2015.10.002
13. X.Q. Wang, X.X. Sun, S.G. Zhou, Microscopic study of higher-order deformation effects on the ground states of superheavy nuclei around ^{270}Hs. Chin. Phys. C **46**, 024107 (2022). https://doi.org/10.1088/1674-1137/ac3904
14. H.L. Liu, F.R. Xu, Y. Sun et al., On the stability of high-k isomers in the second well of actinide nuclei. Eur. Phys. J. A **47**, 135 (2011). https://doi.org/10.1140/epja/i2011-11135-y
15. X.T. He, Z.L. Chen, High-k isomer and the rotational properties in the odd-Z neutron-rich nucleus M^{163}Eu. Chin. Phys. C **43**, 064106 (2019). https://doi.org/10.1088/1674-1137/43/6/064106
16. H.L. Liu, F.R. Xu, P.M. Walker, Understanding the different rotational behaviors of ^{252}No and ^{254}No. Phys. Rev. C **86**, 011301 (2012). https://doi.org/10.1103/PhysRevC.86.011301
17. Z.H. Zhang, J. Meng, E.G. Zhao et al., Rotational properties of the superheavy nucleus ^{256}Rf and its neighboring even-even nuclei in a particle-number-conserving cranked shell model. Phys. Rev. C **87**, 054308 (2013). https://doi.org/10.1103/PhysRevC.87.054308
18. F.F. Xu, Y.K. Wang, Y.P. Wang et al., Emergence of high-order deformation in rotating transfermium nuclei: A microscopic understanding. Phys. Rev. Lett. **133**, 022501 (2024). https://doi.org/10.1103/PhysRevLett.133.022501
19. Z. Łojewski, A. Staszczak, Role of pairing degrees of freedom and higher multipolarity deformations in spontaneous fission process. Nucl. Phys. A **657**, 134–157 (1999). https://doi.org/10.1016/S0375-9474(99)00328-0
20. P. Möller, J. Nix, W. Myers, et al., Nuclear ground-state masses and deformations. At. Data Nucl. Data Tables **59**, 185–381 (1995). https://doi.org/10.1006/adnd.1995.1002
21. M. Bender, P.H. Heenen, P.G. Reinhard, Self-consistent mean-field models for nuclear structure. Rev. Mod. Phys. **75**, 121–180 (2003). https://doi.org/10.1103/RevModPhys.75.121
22. H.L. Wang, Q.Z. Chai, J.G. Jiang et al., Rotational properties in even-even superheavy $^{254-258}$ Rf nuclei based on total-routhian-surface calculations. Chin. Phys. C **38**, 074101 (2014). https://doi.org/10.1088/1674-1137/38/7/074101
23. Q.Z. Chai, W.J. Zhao, M.L. Liu et al., Calculation of multidimensional potential energy surfaces for even-even transuranium nuclei: systematic investigation of the triaxiality effect on the fission barrier. Chin. Phys. C **42**, 054101 (2018). https://doi.org/10.1088/1674-1137/42/5/054101
24. Q. Yang, H.L. Wang, M.L. Liu et al., Characteristics of collectivity along the yrast line in even-even tungsten isotopes. Phys. Rev. C **94**, 024310 (2016). https://doi.org/10.1103/PhysRevC.94.024310
25. Q.Z. Chai, W.J. Zhao, H.L. Wang et al., The triaxiality and coriolis effects on the fission barrier in isovolumic nuclei with mass number $A = 256$ based on multidimensional total routhian surface calculations. Prog. Theor. Exp. Phys. **2018**(5), 053D02 (2018). https://doi.org/10.1093/ptep/pty049
26. J. Yang, J. Dudek, I. Dedes et al., Exotic symmetries as stabilizing factors for superheavy nuclei: Symmetry-oriented generalized concept of nuclear magic numbers. Phys. Rev. C **106**, 054314 (2022). https://doi.org/10.1103/PhysRevC.106.054314
27. Chart of nuclides, National Nuclear Data Center, Brookhaven National Laboratory, http://www.nndc.bnl.gov/chart/
28. A. Lopez-Martens, K. Hauschild, A.I. Svirikhin et al., Fission properties of ^{253}Rf and the stability of neutron-deficient Rf isotopes. Phys. Rev. C **105**, L021306 (2022). https://doi.org/10.1103/PhysRevC.105.L021306
29. I.S. Rogov, G.G. Adamian, N.V. Antonenko, Is there an abrupt fall of spontaneous fission half-lives in ^{248}No and ^{252}Rf? Eur. Phys. J. A **60**, 164 (2024). https://doi.org/10.1140/epja/s10050-024-01382-8
30. F.R. Xu, P.M. Walker, J.A. Sheikh et al., Multi-quasiparticle potential-energy surfaces. Phys. Lett. B **435**, 257–263 (1998). https://doi.org/10.1016/S0370-2693(98)00857-0

31. H.Y. Meng, H.L. Wang, M.L. Liu, Resolution of a possible misinterpretation of the nuclear excitation mode along the yrast line: An investigation on the evolution of rotation and vibration. Phys. Rev. C **105**, 014315 (2022). https://doi.org/10.1103/PhysRevC.105.014315
32. H.Y. Meng, H.L. Wang, M.L. Liu, Landscape appreciation of systematic structure properties in even-even nuclei along the valley of stability. Phys. Rev. C **105**, 014329 (2022). https://doi.org/10.1103/PhysRevC.105.014329
33. W.D. Myers, W.J. Swiatecki, Nuclear masses and deformations. Nucl. Phys. **81**, 1–60 (1966). https://doi.org/10.1016/0029-5582(66)90639-0
34. W. Ryssens, G. Giacalone, B. Schenke et al., Evidence of hexadecapole deformation in Uranium-238 at the relativistic heavy ion collider. Phys. Rev. Lett. **130**, 212302 (2023). https://doi.org/10.1103/PhysRevLett.130.212302
35. J. Dudek, W. Nazarewicz, T. Werner, Discussion of the improved parametrisation of the Woods-Saxon potential for deformed nuclei. Nucl. Phys. A **341**, 253–268 (1980). https://doi.org/10.1016/0375-9474(80)90312-7
36. S. Cwiok, J. Dudek, W. Nazarewicz et al., Single-particle energies, wave functions, quadrupole moments and g-factors in an axially deformed woods-saxon potential with applications to the two-centre-type nuclear problems. Comput. Phys. Commun. **46**, 379–399 (1987). https://doi.org/10.1016/0010-4655(87)90093-2
37. M. Bolsterli, E.O. Fiset, J.R. Nix et al., New calculation of fission barriers for heavy and superheavy nuclei. Phys. Rev. C **5**, 1050–1077 (1972). https://doi.org/10.1103/PhysRevC.5.1050
38. H. Pradhan, Y. Nogami, J. Law, Study of approximations in the nuclear pairing-force problem. Nucl. Phys. A **201**, 357–368 (1973). https://doi.org/10.1016/0375-9474(73)90071-7
39. W. Satuła, R. Wyss, P. Magierski, The lipkin-nogami formalism for the cranked mean field. Nucl. Phys. A **578**, 45–61 (1994). https://doi.org/10.1016/0375-9474(94)90968-7
40. T. Werner, J. Dudek, Shape coexistence effects of super- and hyperdeformed configurations in rotating nuclei with $42 \leq Z \leq 56$ and $74 \leq Z \leq 92$. At. Data Nucl. Data Tables **59**, 1–181 (1995). https://doi.org/10.1006/adnd.1995.1001
41. S.G. Nilsson, C.F. Tsang, A. Sobiczewski et al., On the nuclear structure and stability of heavy and superheavy elements. Nucl. Phys. A **131**, 1–66 (1969). https://doi.org/10.1016/0375-9474(69)90809-4
42. V. Strutinsky, F. Ivanjuk, A new definition of shell corrections to the liquid drop energy. Nucl. Phys. A **255**, 405–418 (1975). https://doi.org/10.1016/0375-9474(75)90688-0
43. K. Pomorski, Particle number conserving shell-correction method. Phys. Rev. C **70**, 044306 (2004). https://doi.org/10.1103/PhysRevC.70.044306
44. A. Gaamouci, I. Dedes, J. Dudek et al., Exotic toroidal and superdeformed configurations in light atomic nuclei: Predictions using a mean-field hamiltonian without parametric correlations. Phys. Rev. C **103**, 054311 (2021). https://doi.org/10.1103/PhysRevC.103.054311
45. J. Dudek, B. Herskind, W. Nazarewicz et al., Pairing, temperature, and deformed-shell effects on the properties of superdeformed ^{152}Dy nucleus. Phys. Rev. C **38**, 940–952 (1988). https://doi.org/10.1103/PhysRevC.38.940
46. S. Bjørnholm, J.E. Lynn, The double-humped fission barrier. Rev. Mod. Phys. **52**, 725–931 (1980). https://doi.org/10.1103/RevModPhys.52.725
47. F.R. Xu, E.G. Zhao, R. Wyss et al., Enhanced stability of superheavy nuclei due to high-spin isomerism. Phys. Rev. Lett. **92**, 252501 (2004). https://doi.org/10.1103/PhysRevLett.92.252501
48. J.F. Wild, E.K. Hulet, R.W. Lougheed et al., Spontaneous fission properties of ^{252,254}No and ^{256,258}[104] and the disappearance of the outer fission barrier. J. Alloys Compd. **213–214**, 86–92 (1994). https://doi.org/10.1016/0925-8388(94)90885-0
49. M. Albertsson, B.G. Carlsson, T. Døssing et al., Calculated fission-fragment mass yields and average total kinetic energies of heavy and superheavy nuclei. Eur. Phys. J. A **56**, 46 (2020). https://doi.org/10.1140/epja/s10050-020-00036-9